

Article

Evaluation of the Ability of SLSTR (Sentinel-3B) and MODIS (Terra) Images to Detect Burned Areas Using Spatial-Temporal Attributes and SVM Classification

Juarez Antonio da Silva Junior ¹, Admilson da Penha Pacheco ¹ , Antonio Miguel Ruiz-Armenteros ^{2,3,4,*} 
and Renato Filipe Faria Henriques ⁵ 

- ¹ Center for Technology and Geosciences, Department of Cartographic and Surveying Engineering, Federal University of Pernambuco, Cidade Universitária, Av. Prof. Moraes Rego, 1235, Recife 50670-901, Brazil
- ² Department of Cartographic, Geodetic and Photogrammetry Engineering, University of Jaén, Campus Las Lagunillas s/n, 23071 Jaén, Spain
- ³ Microgeodesia Jaén Research Group (PAIDI RNM-282), University of Jaén, Campus Las Lagunillas s/n, 23071 Jaén, Spain
- ⁴ Center for Advanced Studies on Earth Sciences, Energy and Environment CEAATEMA, University of Jaén, Campus Las Lagunillas s/n, 23071 Jaén, Spain
- ⁵ Department of Earth Sciences, Institute of Earth Sciences (ICT), University of Minho (UMinho), Campus de Gualtar, 4710-057 Braga, Portugal
- * Correspondence: amruiz@ujaen.es

Abstract: Forest fires are considered one of the major dangers and environmental issues across the world. In the Cerrado biome (Brazilian savannas), forest fires have several consequences, including increased temperature, decreased rainfall, genetic depletion of natural species, and increased risk of respiratory diseases. This study presents a methodology that uses data from the Sea and Land Surface Temperature Radiometer (SLSTR) sensor of the Sentinel-3B satellite and the Moderate Resolution Imaging Spectroradiometer (MODIS) of the Terra satellite to analyze the thematic accuracy of burned area maps and their sensitivity under different spectral resolutions in a large area of 32,000 km² in the Cerrado biome from 2019 to 2021. The methodology used training and the Support Vector Machine (SVM) classifier. To analyze the spectral peculiarities of each orbital platform, the Transformed Divergence (TD) index separability statistic was used. The results showed that for both sensors, the near-infrared (NIR) band has an essential role in the detection of the burned areas, presenting high separability. Overall, it was possible to observe that the spectral mixing problems, registration date, and the spatial resolution of 500 m were the main factors that led to commission errors ranging between 15% and 72% and omission errors between 51% and 86% for both sensors. This study showed the importance of multispectral sensors for monitoring forest fires. It was found, however, that the spectral resolution and burning date may gradually interfere with the detection process.

Keywords: forest fires; remote sensing; Space-Time Equivalence Coefficient (STEC); machine learning



Citation: da Silva Junior, J.A.; Pacheco, A.d.P.; Ruiz-Armenteros, A.M.; Henriques, R.F.F. Evaluation of the Ability of SLSTR (Sentinel-3B) and MODIS (Terra) Images to Detect Burned Areas Using Spatial-Temporal Attributes and SVM Classification. *Forests* **2023**, *14*, 32. <https://doi.org/10.3390/f14010032>

Academic Editors: Rafael Coll Delgado and Rafael De Ávila Rodrigues

Received: 24 November 2022

Revised: 18 December 2022

Accepted: 21 December 2022

Published: 24 December 2022



Copyright: © 2022 by the authors. Licensee MDPI, Basel, Switzerland. This article is an open access article distributed under the terms and conditions of the Creative Commons Attribution (CC BY) license (<https://creativecommons.org/licenses/by/4.0/>).

1. Introduction

A new understanding of how the biota responds to fire events is extremely relevant for the management and conservation of terrestrial ecosystems, especially in the face of global environmental changes and the increase in human activities [1]. Vegetation burning is a global-scale process that affects the distribution of major biogeochemical cycles and the climate system [2]. The increase in the occurrence and frequency of extreme droughts has led to an increase in the number of disasters associated with forest fires across the planet [3]. Burning, in addition to altering soil moisture as a function of changes in infiltration rate and transpiration rate, can consequently alter the soil water stock [4].

The Cerrado biome (Brazilian savannas) occupies an area of 2.03 million km², about 22% of the national territory, being the second-largest biome in South America, observed in

the northern, north-eastern, south-eastern, and midwestern regions [5,6]. Cerrado is also the second-largest biome in Brazil and one of the most species-rich savannas in the world [6]. Currently, the Cerrado biome is under threat from increased human pressure, which has led to the accelerated conversion of natural ecosystems into areas for cultivation, pastures, and infrastructure development [7]. These changes in land use and cover have resulted in various environmental impacts, including loss and fragmentation of the natural habitat, increasing the risk of species extinction and affecting the hydrological cycle, biogeochemical processes, and ecosystem function [8]. Fire events are a common and decisive phenomena in the Cerrado vegetation, which has greatly contributed to the evolution of its flora [9]. These changes in the fire regime contribute to increased fire frequency and intensity, affecting the ecosystem's resilience.

The Sea and Land Surface Temperature Radiometer (SLSTR) from Sentinel-3 and Moderate Resolution Imaging Spectroradiometer Sensor (MODIS) from the Terra satellite sensors are some of the most commonly used Earth Observation Satellite (EOS) sensors for detecting, monitoring, and evaluating forest fires on a regional and global scale [10]. Varying spatial and temporal resolutions of EOS sensors are a critical issue for fire detection. Satellite revisit frequency and time often affect the effectiveness of emergency monitoring. A practical alternative solution is to combine several sensors of different spatial and temporal resolutions to produce fast and reliable estimates of the location and extent of forest fires in tropical zones. Reducing the time needed to identify wildfires can lead to increased situational awareness as well as faster decision-making by fire control teams [11], thus reducing the potential negative impact that a fire outbreak could have in areas with high biodiversity and fragile ecosystems (e.g., the Cerrado and Amazon biomes).

Global burned area products from the MODIS sensor, aboard the Terra and Aqua satellites provided by the National Aeronautics and Space Administration (NASA), were used to estimate global emissions, with a coarse ground sampling distance (GSD) (500 m/pixel) and a specification of 15 days available for download worldwide [12–14]. The SLSTR sensor attached to Sentinel-3A and 3B satellites is the latest addition to the range of in-orbit optical sensors launched by the European Space Agency (ESA) in February 2016 and April 2018, respectively. These twin satellites provide images with a GSD of 500 m/pixel and a range of 1420 km in visible (VIS), infrared (IR), and thermal (TIR) wavelengths, with a temporal resolution of 1 day at the equator, giving high potential for rapid detection and tracking of forest fires, as well as for the systematic monitoring of the recovery process of burned areas [11,15,16]. MODIS is widely used in the Cerrado for mapping burned areas [17], active fire detection [18], forest fire product quality [19,20] and carbon fluxes [21], spectral indices, and time series analysis [22–24]. Despite recent research on the use of the SLSTR in the context of forest fires, it has not yet been used exclusively in the Cerrado biome; on the other hand, it has been successfully applied in some countries in the southern hemisphere [11,25]. These products, however, are not suitable for the identification of small burned areas due to their spatial resolution [26]. Despite the increasing frequency and intensity of fire events in the Cerrado biome, the products of the burned area and studies conducted using medium and high spatial resolution are limited to local estimates or simply to a specific year [27,28]. Automatic mapping for burned areas using images of different spatial and spectral resolutions and cloud computing is not yet available and is still a scientific challenge.

The validation of remote sensing products provides critical information to help users determine if the data meet their needs and benchmark algorithm improvements. The Earth Observation Satellite Working Group on Calibration and Validation (<https://lpvs.gsfc.nasa.gov/>) (accessed on 15 October 2022) defines validation as the process of independently evaluating the quality of data products derived from the system. Hawbaker et al. [29] recommend, for the validation of coarse-resolution global burned area products, the collection of reference data from images that: (a) have higher spatial resolution and sufficient spectral resolution to identify burned areas; (b) span the time period of products being validated; and (c) can be paired to separate recently burned areas from older burned areas,

avoiding confusion with other types of changes. Validation of global coarse-resolution burned area products following these protocols typically uses pairs of Landsat images to develop reference data [30].

The methods used to generate burned area products from optical satellite images are numerous and can be categorized according to various aspects. For example, object- or pixel-based approaches; the use of a post-fire scene only (monotemporal approach) or the additional integration of pre-fire data and/or time series (multitemporal approach); and the classification algorithms applied, such as Random Forest [31], Support Vector Machine [32], or K-Nearest Neighbor [33]. More recently, there have been major efforts to automate the process of classifying/mapping specific targets using Deep Learning algorithms, described in LeCun et al. [34] as the Deep Neural Network (DNN), which includes a learning algorithm based on an artificial neural network.

This study describes the spatial and spectral capabilities and limitations of SLSTR and MODIS sensors in relation to observations of burned areas, pioneered in the Cerrado biome, analyzing the quality of their detection through the parameters of thematic precision, time sensitivity, and fire size. This study aims to establish a supervised methodological approach to analyze the thematic accuracy of the detection of burned areas in a large portion of the Cerrado biome, in three fires during the dry period from 2019 to 2021. For that, we used Support Vector Machine (SVM) and images of the same spatial resolution and different spectral resolutions from the Sentinel-3/SLSTR and Terra/MODIS satellite sensors and compared them to official burn mapping products. The application of Machine Learning to this spatial data analysis will benefit researchers, managers, and users of environmental agencies.

2. Materials and Methods

2.1. Materials

2.1.1. Study Area

The study area comprises the extension of the Landsat orbit/point grid (221/66) with approximately 32,000 km², fully inserted in the Brazilian state of Piauí and located in the Cerrado biome, close to the Caatinga biome (Figure 1).

According to Embrapa [35], Cerrado is the richest tropical savannah in the world because it contains about 5% of all the diversity on the planet. The Cerrado is home to 30% of the different living beings identified in Brazil, where its flora is composed of 12,385 plant species and 4400 of them are endemic [35]. Cerrado is the biome with the highest number of active fires detected in Brazil, losing to the Amazon biome. For example, in 2020, 631,800 hotspots were detected in Cerrado, representing approximately 28.16% of the total hotspots observed in Brazil [36]. According to the Instituto Nacional de Pesquisas Espaciais (INPE) [36], most active fires occur between June and November, the period with the lowest amount of precipitation received. In the dry season, the risk of fire propagation and dispersion is expected to increase, affecting nearby forest areas and causing forest degradation, which is an important source for the REDD+ (Reducing Emissions from Deforestation and Forest Degradation) program (<https://redd.unfccc.int>, accessed on 15 October 2022), since these areas remain as forest areas, but with great loss of ecosystems [36].

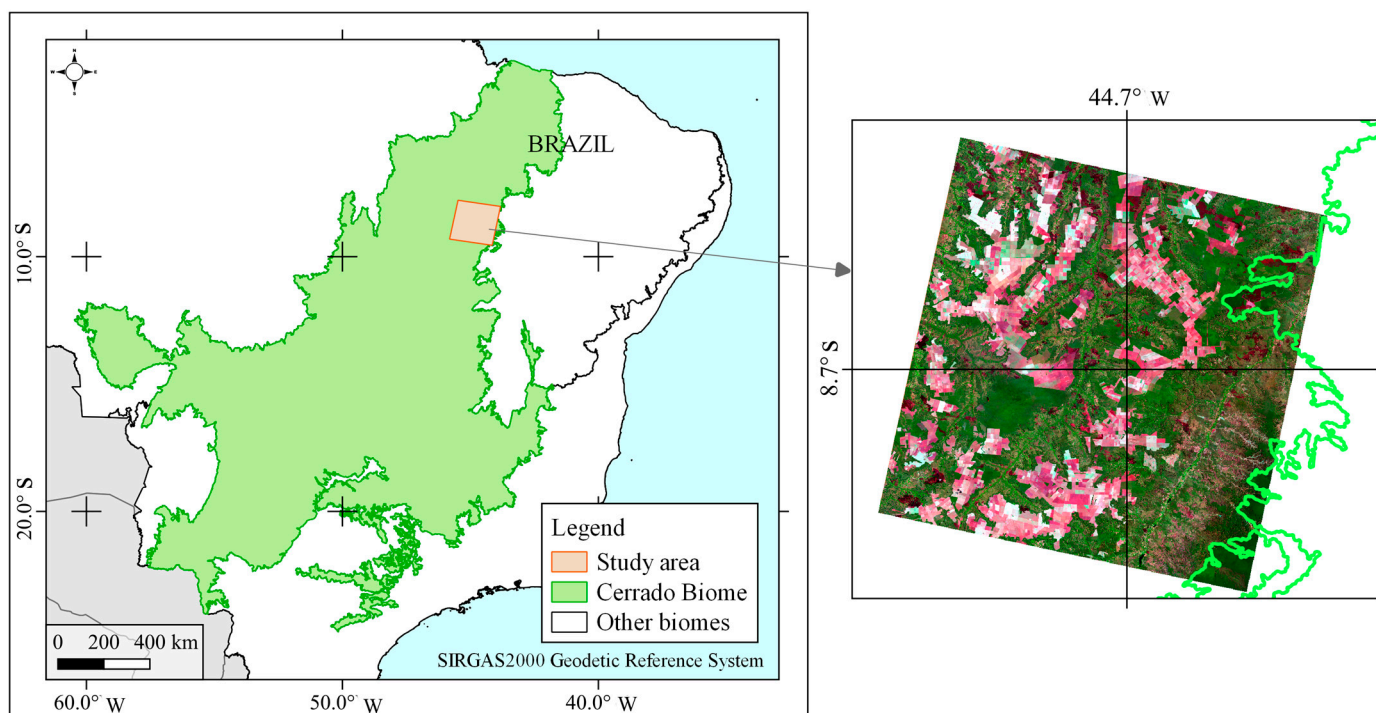


Figure 1. Location of the study area in the south of the state of Piauí and in the north of the Cerrado biome (Brazil) (coordinates in WGS84—EPSG:4326).

2.1.2. Satellite Data

In order to generate maps of spatial distribution and spectral detection of the burned area, three pairs of images from orbital sensors were used, such as the SLSTR and MODIS/Surface Reflectance 8-Day L3 Global (MOD091A1), aboard the Sentinel-3A and Terra satellites, respectively.

The SLSTR is a dual-scan temperature radiometer in low Earth orbit (800–830 km altitude), aboard the Sentinel-3 satellite RBT-1B mode. It employs the scanning technique along the dual vision range (nadir and backward oblique) for 9 channels in the VIS, TIR, and shortwave infrared (SWIR) spectrum (Table 1). The Level 1B pre-processing bands include the calculation of radiometric measurements for each SLSTR channel and various tests relating to surface signaling, clouds, determination of pixel properties, geographic position, 500 m spatial resolution, and a revisit period of 1.9 days at the equator [37]. In this study, the SLSTR images were made available through the Sentinel Data Hub platform (<https://scihub.copernicus.eu/>, accessed on 15 October 2022) for the months between September and October of the years 2019 to 2021 (Table 2). SLSTR data in 1B-RBT mode were converted from radiance to ToA (Top of Atmosphere) reflectance using the software SNAP 8.0. Due to noise problems found in the S4 band for all years, this band was removed from the analyses.

Table 1. Characteristics of the images obtained by the MODIS (MOD09A1) and SLSTR (RBT-1B) sensors used in this study. Source: adapted from Vermote [38] and Sentinel-3 [37] (<https://sentinel.esa.int/web/sentinel/user-guides/sentinel-3-SLSTR>, accessed on 15 October 2022).

Spectral Band	Spectral Resolution (nm)		Spatial Resolution (m)
	MOD09A1	SLSTR	
Blue	459–479	-	500
Green	545–565	530–570	
Red	620–670	630–670	
NIR	841–876	840–880	
SWIR1	1230–1250	-	
SWIR2	1628–1652	1550–1670	
SWIR3	2105–2155	2200–2300	

Table 2. SLSTR and MODIS image dates and Aq30m data.

SLSTR	MODIS	Aq30m
16 September 2019	21 September 2019	22 September 2019
16 September 2020	15 October 2020	17 September 2020
21 October 2021	15 October 2021	21 October 2021

Additionally, in the same time range as the SLSTR data (Table 2), scenes from the MODIS sensor obtained from the surface reflectance product MOD09A1, made available by the Distributed Active Archive Center of the Oak Ridge National Laboratory (ORNL DAAC) (Global Subset Tool) were used: MODIS/VIIRS Land Products (<https://modis.ornl.gov/cgi-bin/MODIS/global/subset.pl>, accessed on 15 October 2022). These data have a spatial resolution of 500 m and provide spectral surface reflectance of the MODIS/Earth bands 1–7 (Table 1) corrected for atmospheric conditions (e.g., gases, aerosols, and Rayleigh scattering) at 8-day intervals. The criteria for choosing the pixel include cloud and solar zenith. When the various acquisitions met the criteria, the pixel with the minimum value of channel 3 (blue) was used [38]. The satellite image dates and the reference data for each of the three selected burned areas (Aq30m) are presented in Table 2.

2.2. Methods

2.2.1. Separability Analysis

Statistical separability indices are statistical measures to quantify the separability of membership and non-membership classes under different bands or spectral indices [39]. Several separability statistics are used in remote sensing, for example, the Jeffries–Matusita (JM) and Transformed Divergence (TD) indices. In this study, the separability between classes was calculated using TD statistics [40]. The highest value in particular, on a scale of 0 to 2, denotes high dissimilarity between the burned and unburned classes. A value of less than 1 indicates low spectral correspondence between the classes [41]. The TD index is a commonly used form of separability measure designed to predict the best channel combinations for the multispectral classification of terrestrial features [40–42]. This separability statistic uses a saturating transformation to reduce the dimensionality of the datasets and provide information on the relative degree to which burned areas can be accurately classified against the spectral bands of the SLSTR and MODIS sensors.

The TD statistic also provides insight into which channels can be used to obtain the best classification results and quantify the separability of burned and unburned areas. Therefore, it is based on the weighted covariance distance between the class means to determine whether the class signatures are separable [42], through Equation (1):

$$TD = 2 \left[1 - \exp \left(-\frac{D}{8} \right) \right], \quad (1)$$

$$D = \frac{1}{2} \text{tr} \left[(C_1 - C_2) (C_1^{-1} - C_2^{-1}) \right] + \frac{1}{2} \text{tr} \left[(C_1^{-1} - C_2^{-1}) (\mu_1 - \mu_2) (\mu_1 - \mu_2)^T \right]$$

where TD is the Transformed Divergence between class 1 and class 2, C_1 and C_2 are the covariance matrices of class 1 and class 2, μ_1 and μ_2 are the average vectors of class 1 and class 2, tr is the matrix trace function, and T is the matrix transposition function. The separability calculation was performed in the RStudio Desktop software (Version 1.4.1717) using the 'spatialEco' package [43].

2.2.2. Training and Classification by Support Vector Machine (SVM)

SVM is based on statistical learning theory and aims to determine the location of decision limits that produce optimal class separation [44]. According to Vapnik [44], in the case of a two-class pattern recognition problem in which the classes are linearly separable, among the infinite number of linear decision limits, SVM selects the one that minimizes the generalization error. Thus, the decision boundary selected will be the one that leaves the largest margin between the two classes, where the margin represents the distance between the hyperplane and the support vectors. SVM analysis attempts to position the margin so that the space between it and the SVM support vectors is maximized [44]. The data points closest to the hyperplane are used to measure the margin; therefore, these data points are called 'support vectors' [44]. If the two classes are not linearly separable, SVM tries to find the hyperplane that maximizes the margin while minimizing an amount proportional to the number of misclassifications [45]. In general, SVM works by considering each pixel as a vector in a multidimensional system, where each class has a pixel as a support vector to establish the class boundary. When the data do not fit an obvious hyperplane, the point of view must be shifted to a higher dimensional space. In this way, SVM allows users to choose a kernel function that best suits the data they are working with.

In studies of the classification of burned areas, according to Dragozi et al. [46] and Pereira et al. [47], the Radial Base Function (RBF) kernel of the SVM classifier is commonly used and performs well. Therefore, in this study, the RBF kernel was used to implement the SVM algorithm, although there are two parameters that need to be configured when applying the SVM classifier with the RBF kernel: the optimal cost parameters (C) and the kernel width parameter (γ), also called "gamma" [48]. Parameter C decides the size of the classification error allowed for non-separable training data, which makes it possible to adjust the rigidity of the training data. The kernel width parameter (γ) affects the smoothing of the shape of the class division hyperplane [49]. Larger values of C can lead to an overfitting model while increasing the value of γ will affect the shape of the class division hyperplane, which can affect classification accuracy results [50].

To perform the classification, a training set is needed to allow the classifier to learn the process through examples that indicate the correspondence between a training sample and a class [51]. Following the studies by Li et al. [52] and Noi and Kappas [50] to find the ideal parameters for SVM, five values of C (1, 5, 10, 50, 100) and four values of γ (0.1, 1, 5, 10) were selected. The best pre-established C and γ combination was evaluated with the number of iterations from 1 to 1000. Finally, the SVM classification was performed for the entire SLSTR and MODIS dataset using the best values of the trained hyperparameters. The selection of training samples was performed in the QGIS 3.10 software. Hyperparameter and classification tests were performed in the RStudio Desktop 1.4.1717 software using the package 'e1071' [53].

2.2.3. Validation

The validation of remote sensing data is usually based on measurements taken from field campaigns, which are viewed as a reference on-site. In many cases, the validation process is carried out by remote sensing products provided by official institutions or by sensors with high spectral and spatial resolution.

In this work, the reference validation product was the annual burned area in the years 2019 to 2021 from the database made available by the National Institute for Space Research (INPE) through the INPE Fire Database (BDQueimadas—Aq30m) available at

<http://queimadas.dgi.inpe.br/queimadas/aq30m/>, accessed on 15 October 2022. Data were made available in vector polygon format covering the entire study area.

This monitoring uses images from the Landsat series with 30 m spatial resolution, which operationally and automatically estimates the burned surface, generating digital maps, temporal comparisons, and products to support the management and assessment of the impact of the use of fire on vegetation. The period of the images used for SLSTR and MODIS was carefully chosen in accordance with the data (Aq30m) to be as short as possible and, as shown in Table 2, considering that this parameter depends on the imaging cycle of the satellites, avoiding possible spatial inconsistencies due to changes in the burn scar and ground cover. However, problems with clouds were the main cause for time intervals different from those recommended by the literature (29 days) [17].

2.2.4. Accuracy Analysis

The quality of a given thematic map, which is derived from remote sensing data, is generally evaluated by systematic comparison with other maps also derived from remote sensing. The quality assessment is generally performed on the basis of verification measures derived from confusion matrices [54]. The cross-tabulation approach is the most common way of assessing thematic accuracy. In this context, a comparison and analysis of the quality of the maps of burned areas obtained by the SLSTR and MODIS images in the years 2019 to 2021 were carried out.

The polygon of the burned area obtained from the BDQueimadas map was used as a spatial reference in this study for analysis in a confusion matrix. Following the terminology presented by Fawcett et al. [55], baseline data (true class) were referred to as positive (burned) or negative (unburned). The omission errors (OE) and commission errors (CE) provide information about the reliability and discrimination power of the developed classifier. For these statistics, an inconsistent ranking exhibits a trend value equal to 0%, while a higher trend (reaching 100%) indicates that the events were ranked well. The Dice Coefficient (DC) ranges between 0 and 1 and measures the overlap fraction of pixels classified as burned to those actually burned in the reference map [17].

2.2.5. Regression Analysis by Proportion of Burned Area in 5 × 5 km Cells

A certain degree of OE and CE is due only to the presence of mixed pixels [56] and the confusion matrix does not distinguish between these unavoidable errors due to misclassification [26]. For this reason, the confusion matrix and derived accuracy metrics were complemented by a regional scale accuracy assessment, based on regression metrics. The proportion of 5 km resolution grid cells detected as burned by the SLSTR and MODIS products is compared to the proportion of area detected by the reference data; the slope and displacement of the regression line are indications of the accuracy of detection of the burned area, while the coefficient of determination (R^2) is an indication of the precision [26].

2.2.6. Space-Time Equivalence Coefficient (STEC)

To assess the daily recurrence of errors in classification in relation to periodicity with the reference product, the Space-Time Equivalence Coefficient (STEC) was implemented (Equation (2)). This coefficient is capable of measuring the stability of spatial errors in relation to the recording time of data obtained by remote sensing, using the usual elements of confusion matrices in binary cases, through adaptations of normalization precision equations found in Strötgen [57] and Barsi et al. [58].

$$\text{STEC} = \ln(\text{TP}) * \sqrt{\frac{\ln(a*FN*b*FP)}{\ln(\Delta t + 1)}} \quad (2)$$

when the test product date is n days before that of the reference product, then $a = \ln(n)$ and $b = 1$ and when the test product date is n days after the reference product date, then $a = 1$ and $b = \ln(n)$. If the difference between dates is one day before or after the reference date then

$a = 1$ and $b = 1$. True positive (TP) is the test result that correctly indicates the presence of a condition or characteristic, False negative (FN) is the test result that erroneously indicates that a specific condition or attribute is absent, False Positive (FP) is the test result that erroneously indicates that a specific condition or attribute is present, and Δt is the number of days between the evaluation data and the reference data ($\Delta t \neq 0$ and $\Delta t < 0$). The STEC ranges from 0 to 2. Values below 1 are considered to be low interference from time in relation to spatial errors and values above 1 are considered to be high interference from time in relation to spatial errors. Values above 2 are considered discrepant; in this case, it is recommended to perform the analysis with the smallest possible Δt .

In this article, the analysis is based exactly on the Δt between the recording of the SLSTR and MODIS images and the date marked on the Aq30m reference product, and, additionally, on a variation of 30 days, since the fire response in the land cover of the Cerrado biome can persist up to 30 days after the fire.

3. Results

3.1. Separability Analysis for SLSTR and MODIS Bands

Initially, the separation between burned and unburned areas in the different bands of SLSTR and MODIS was evaluated, as shown in Figure 2. It was observed that different bands presented different separability performances.

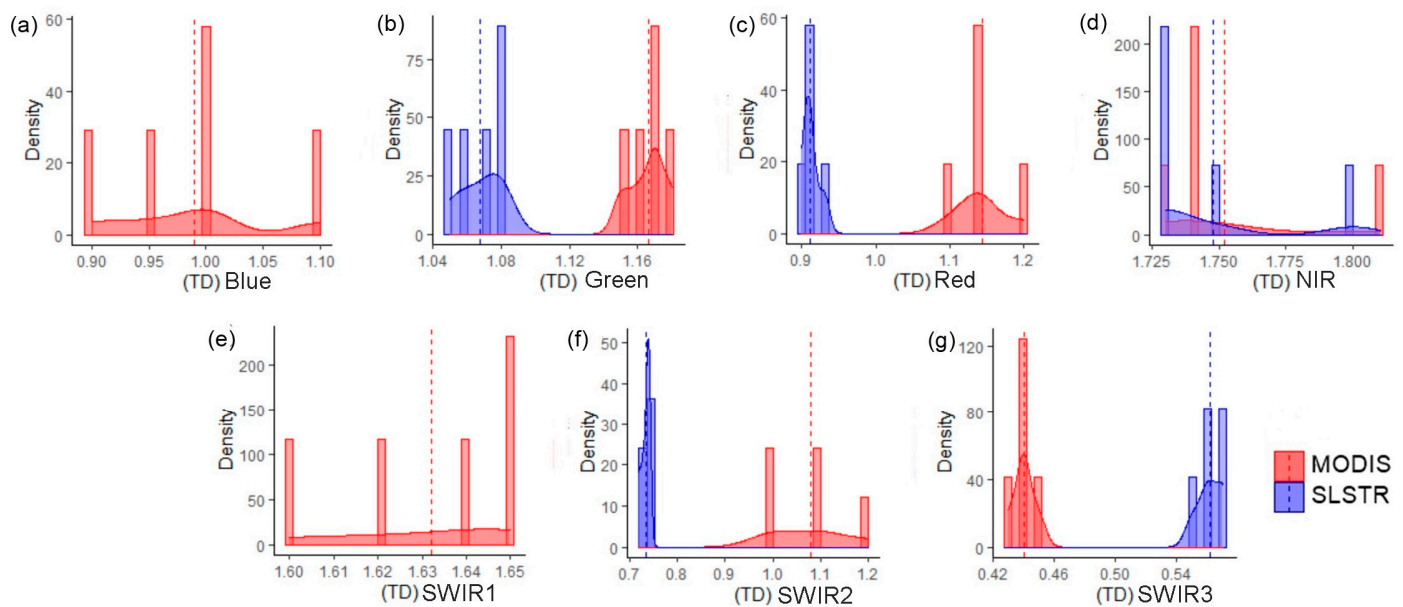


Figure 2. Separability values for the SLSTR (red) and MODIS bands (blue). (a) Blue, (b) Green, (c) Red, (d) NIR, (e) SWIR1, (f) SWIR2, (g) SWIR3.

Note that for the VIS bands, there was a lower discriminatory power, with separability estimates below 1 (except for the MODIS red band), although for the SLSTR green band, the separability estimates were slightly higher. The NIR band, as expected, showed a high estimate of separability in both sensors, with values above 1.7, even in the MODIS NIR band. For MODIS, in the SWIR range, it presented higher separability performance in relation to the SLSTR and the VIS bands, thus enhancing its ability to detect burned areas, although estimates have focused on values below 1.2. Overall, the reflectance in SWIR1 decreases after burning, due to the removal of water-retaining vegetation by fire [59]. For longer wavelength bands (SWIR1), the spectral reflectance of unburned dry vegetation (proportion of green vegetation absorbing radiation due to water content) and burned surfaces can be equally high, increasing the separability estimate (higher values of TD).

3.2. Effects of Adjustment Parameters on Classification Precision

The test results to find the best parameters of the SVM classifier of the combination C and γ of the RBF function, as well as the number of iterations in relation to the squared error in the pre-classification process of the burned area, are presented in Figures 3 and 4. The analysis was based on the training samples extracted from the satellite datasets. This type of analysis of adjustment of the classification model is important since it allows users to know and simultaneously change the flexibility of the classification limits of the SVM model.

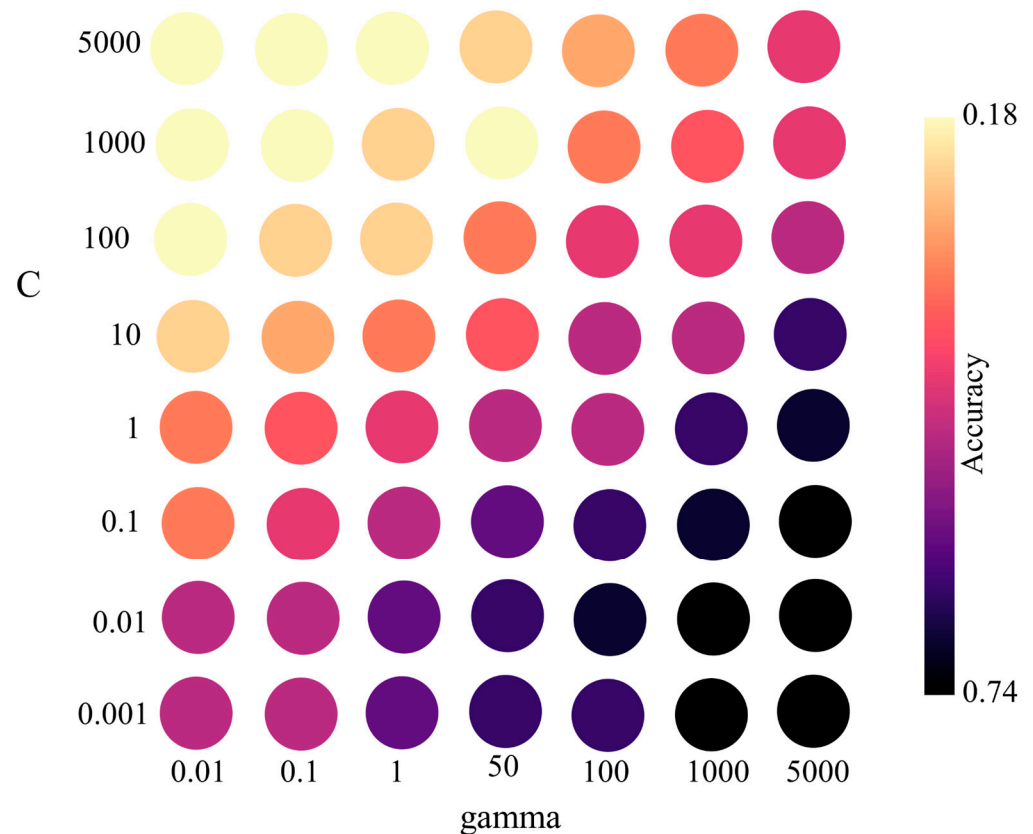


Figure 3. Relation between accuracy and parameters (C and γ) of the SVM classifier obtained from data subsets of training samples.

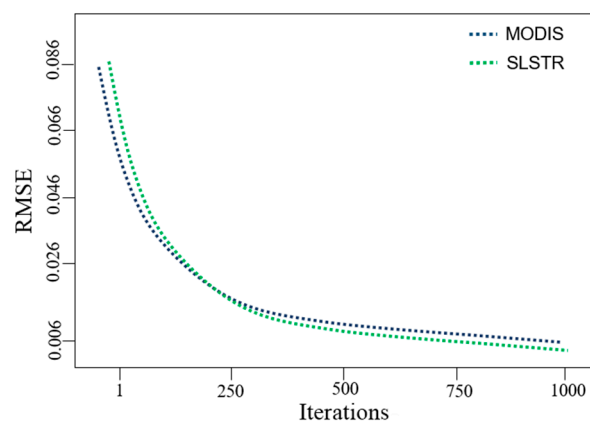


Figure 4. Relationship between the root mean square error (RMSE) and the number of iterations for the parameters (C and γ) for pre-establishment of the SVM classifier obtained from different subsets of training sample data.

The results obtained in Figure 3 show that the accuracy is weakly influenced by the variable C and is very sensitive to the gamma parameter. Decreasing gamma (increased complexity) to training accuracy monotonously increased up to 100%, that is, up to the perfect precision model. Considering the dependencies presented in Figure 3, it can be assumed that the selection of adequate and optimal values of the gamma and C coefficients consists of which validation accuracy is the highest with the most effective possible training model. In this case, among the configurations with the highest learning accuracy, the best hit value was obtained for the gamma parameter equal to 1000 and C parameter equal to 0.001. Therefore, these values were considered optimal. Thus, they are used as input parameters in the classification process.

The behavior of the dataset presented corroborates the theory of Mountrakis et al. [60] and of Bahari et al. [61]. For a very large gamma, the radius of the area of influence of the support vectors includes only the support vector itself and no regularization with C, being able to avoid overfitting. This produces more segmented boundaries, which are narrower around the support vectors. The predictor is therefore more likely to fit all of them. Then, the final evaluation metrics of the model were iteratively adjusted from 1 to 1000 times.

Figure 4 shows that the highest iteration number resulted in the lowest error estimates for both data sets. In this way, more iterations cover a wider search space and reduce the chances of overfitting, although this causes an increase in execution time. Therefore, a number of iterations in which there was a low variation or stabilization of the training error was chosen, that is, 1000 iterations, where the lowest RMSE estimate based on this number in the determined interval is found.

3.3. SLSTR and MODIS Accuracy Analysis

After the SVM classification and comparison with the reference data, Figure 5 shows the spatial distribution of OE and CE for the classification of burned and unburned areas for the SLSTR and MODIS sensors.

It can be seen in Figure 5 that MODIS obtained more consistent OE and CE than SLSTR. For MODIS, the largest CE estimate was found for the year 2020 (56%), reaching 568.6 km² of area incorrectly classified as burned. In 2019, it presented the lowest estimate (15%), with an overestimation of 92.2 km². For the SLSTR, the largest CE were also found in 2020 (72%).

The OE exceeded the CE, which was already expected since the reference data were dated on the same day and after the MODIS and SLTR detection, in addition to the finer spatial resolution (30 m), where smaller burned areas (25 km²) were not detected by the coarser resolution sensors (500 m/pixel GSD). The maps generated by the SLSTR sensor showed the largest OE, reaching values above 80% for the year 2020, with approximately 2872.60 km² of areas incorrectly classified. In general, MODIS presented slightly lower values of OE in relation to SLSTR.

The results found confirmed the findings of previous studies in the Cerrado biome on the underestimation of burned areas from global remote sensing due to the omission of small fires that often occur mainly close to agricultural areas. Table 3 shows the Dice Coefficient values.

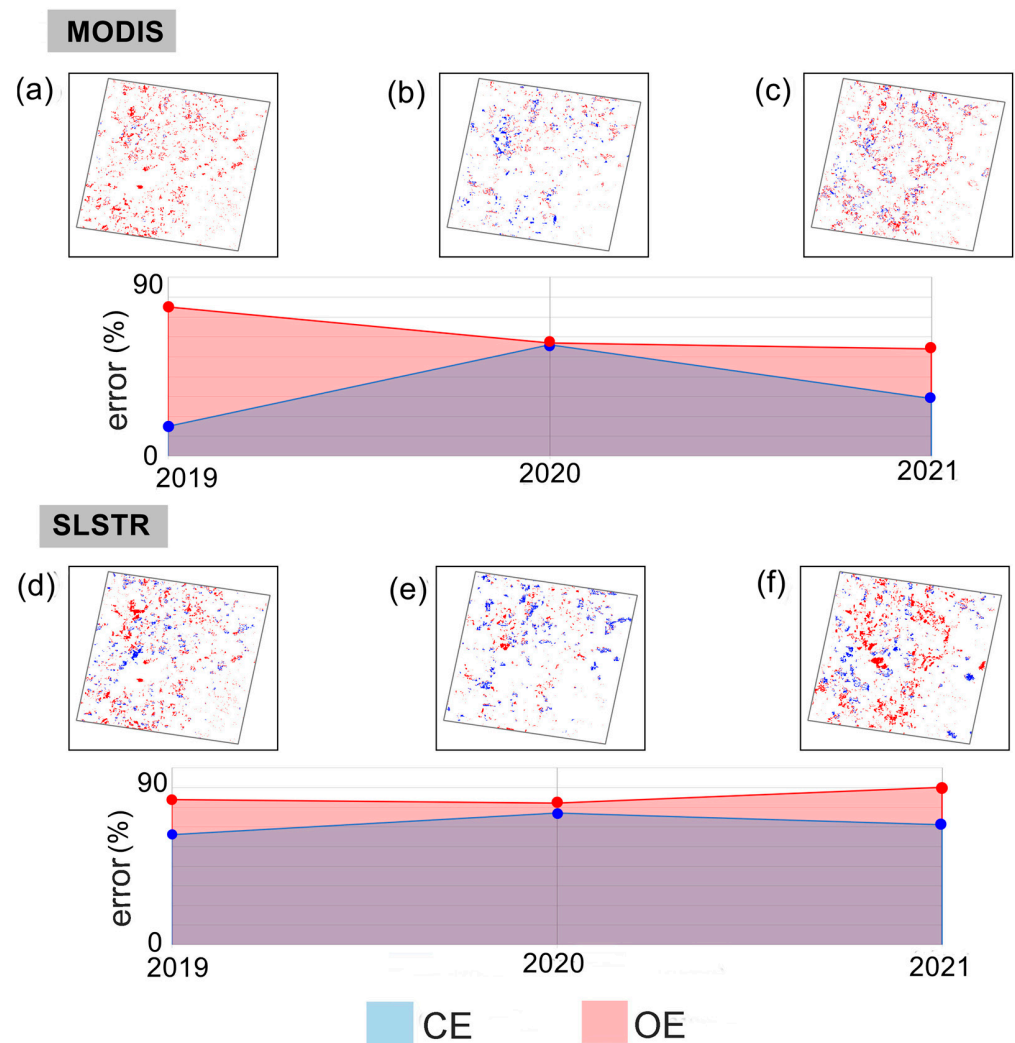


Figure 5. Spatial distribution of OE and CE for the burned area maps generated by the SVM classifier in the SLSTR and MODIS images for years 2019 (a,d), 2020 (b,e), and 2021 (c,f).

Table 3. Data Coefficient (DC) Values after validation of MODIS and SLSTR burned area maps.

Period	MODIS	SLSTR
2019	0.38	0.33
2020	0.43	0.30
2021	0.56	0.26

The DC presented values in agreement with the errors, with the lowest estimates for the SLSTR sensor. However, it is important to note that MODIS also presented low estimates, with a small increase for the year 2021 (0.56), in total disparity with the same year for the SLSTR sensor, which presented the lowest estimate of the dataset (0.26). Overall, MODIS had an average DC of 0.45 and SLSTR of 0.29.

In general, the classifications present low estimates of DC coefficient as summarized in Table 3; that is, there was a discontinuous adherence with the reference data for the class of presence of burned area since this parameter is quite sensitive to false alarms and missing pixels. The values found for the DC coefficient allow us to partially summarize that in the annual variability in the OE/CE of the annual maps of burned areas from SLSTR and MODIS, for the entire data series, MODIS obtained an average OE and CE of 60% and 34% and the SLSTR of 60% and 76%, respectively.

3.4. Proportion of Burned Areas per 5×5 km Cells

Considering the coefficients of determination of the estimated regression lines, it is possible to observe the highest correlations for MODIS in relation to SLSTR (Figure 6), highlighting the year 2019, both with an accuracy of $R^2 = 0.49$. This shows greater spatial adequacy of MODIS with the reference data, mainly for the largest and densest scars (>25 km²), compensating for CE and OE.

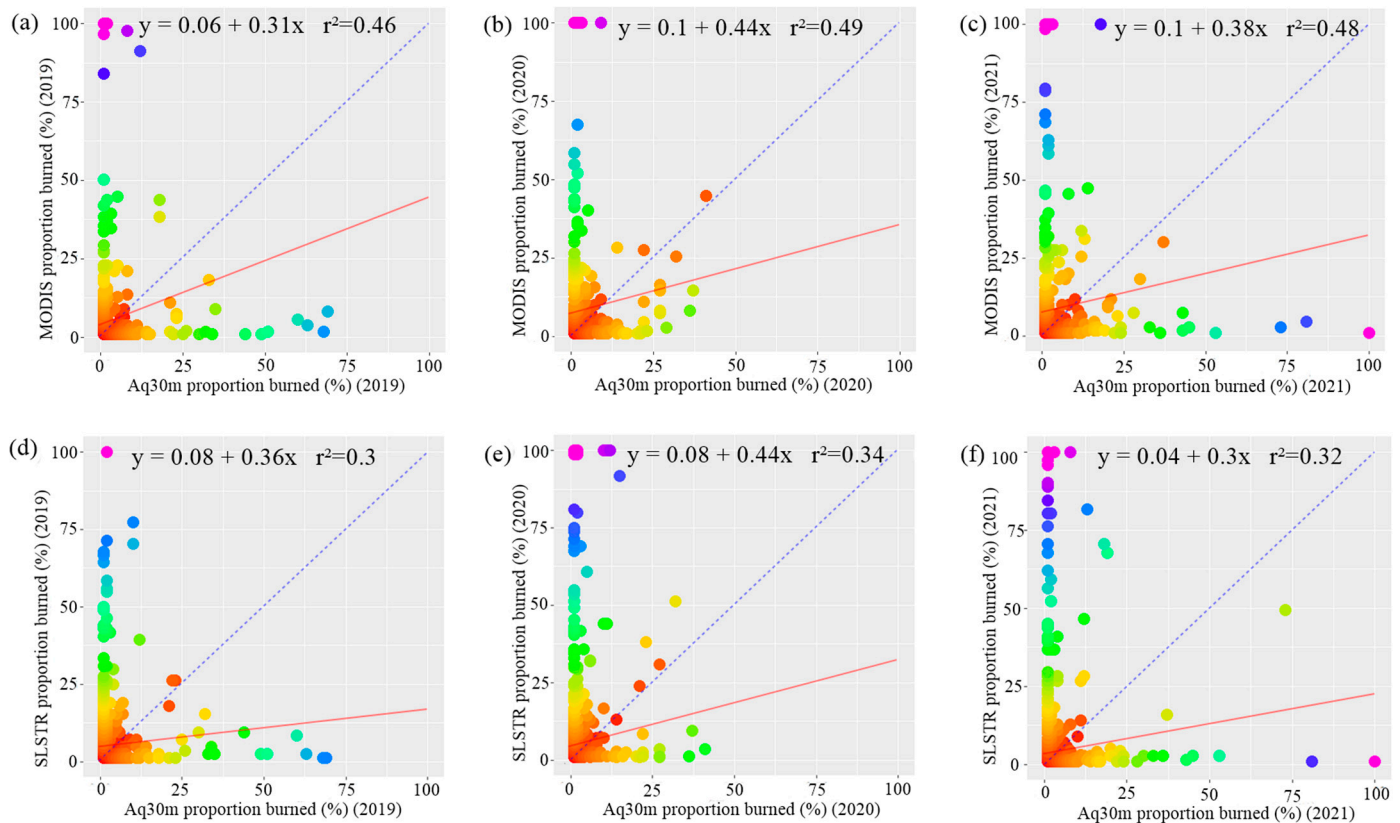


Figure 6. Regressions of the proportion of burned area in each 5×5 km square grid of the maps generated by the SLSTR and MODIS sensors and the reference map derived from the Aq30m during the fire season for the years (a,d) 2019, (b,e) 2020, and (c,f) 2021.

According to Figure 6, all linear regressions were significant for $p < 0.05$, according to the Student's t -test. For the SLSTR, the accuracies were concentrated between 0.3 and 0.34, and the highest coefficient of determination was found for the year 2020 ($R^2 = 0.34$), in accordance with the lowest estimates of EC and OE shown in Figure 5. The slopes of the regression lines are similar in both sensors, although for MODIS, the slopes were slightly higher and, added to the positive intercepts, indicate that, for a cell size of 5 km², the maps generated by MODIS correctly mapped a larger proportion of the burned landscape in the study area. In the burned areas detected by MODIS, approximately 89% of the cells presented values lower than 5 km²; for the SLSTR it was 77%. This indicates patterns of burned area corresponding to small scars in greater numbers, probably leading to a decrease in spatial adherence with Landsat data.

3.5. Assessment of Spatial-Temporal Sensitivity in Fire Detection Based on the STEC Coefficient

Figure 7 shows the sensitivity of the spatial detection of the burned area in relation to the temporal discrepancy between the SLSTR and MODIS imaging date with respect to the reference product based on the STEC coefficient. The orbital sensors are represented with a red dashed line and the average 30-day STEC coefficient with a blue dashed line.

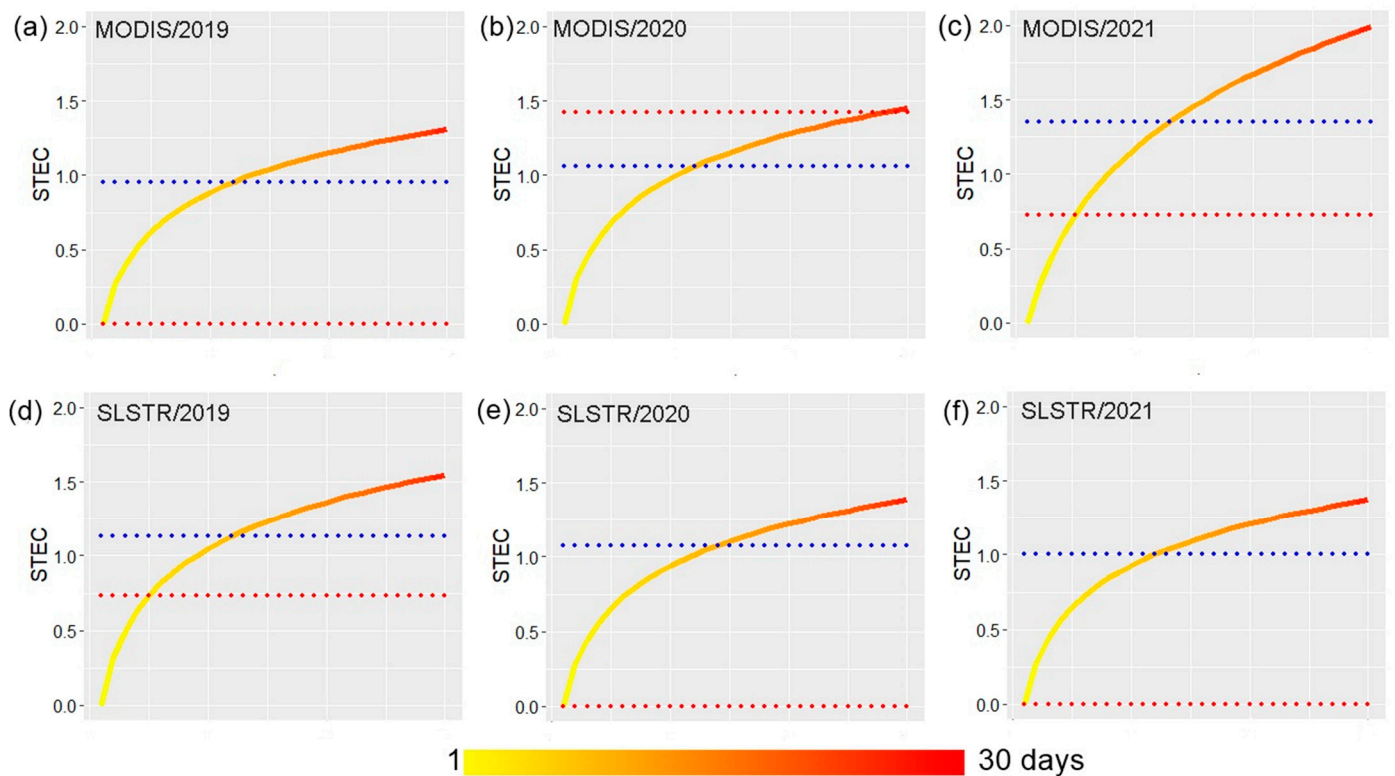


Figure 7. Detection of SLSTR and MODIS burned areas through the daily and average 30-day STEC coefficient. Red dashed line represents the sensor and the blue dashed line the average 30-day STEC coefficient. (a,d) for 2019, (b,e) for 2020, and (c,f) for 2021.

The schematic graphs of the daily STEC coefficient showed a significant variation between the years, with the highest values seen for MODIS in the years 2020 (1.42) and 2021 (0.72). The SLSTR had more stable daily STEC coefficient values, especially for the year 2019 (0.64). The better performance of SLSTR was expected since its Δt was slightly lower compared to MODIS. On the other hand, the average STEC coefficient showed stable values close to 1.0 for both sensors, mainly the SLSTR, which may be related to the mismatch between the low Δt and the high OE and CE found for this sensor. Only MODIS/2021 showed a slightly higher average STEC value (1.35), corresponding to high detection errors, even with a Δt of 5 days.

3.6. Analysis of the Accuracy and Linear Regression by Proportion 5×5 km for Small and Large Fires in the Year 2021

Due to the importance of remote sensing forest fire analysis and to establish a relationship between fire size and detection errors, OE and CE were shown in Figure 8 based on small fires (<5 km²) and large fires (>5 km²) for the year 2021 for the SLSTR and MODIS maps (Figure 5).

For large fires (>5 km²) a CE of 46% and an OE of 31% were marked for MODIS, which represent approximately 831.3 km² of correct classification and a DC coefficient of 0.64. SLSTR presented slightly higher error estimates compared to MODIS, with a CE of 78%, OE of 67%, and a DC coefficient of 0.28. In spatial terms, even for the SLSTR, the estimates resulted in an underestimation of the burned area of approximately 1203.63 km² and an accuracy of 332.78 km², corresponding to a percentage difference of 43% in relation to the total area mapped, with MODIS showing a difference of 56%.

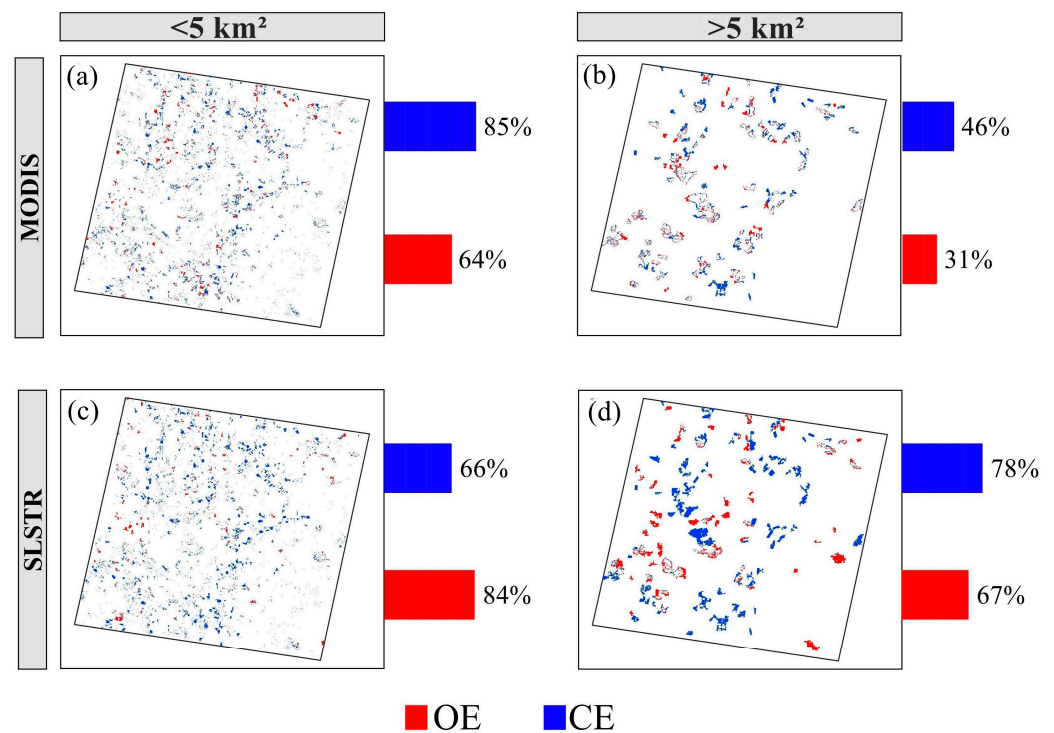


Figure 8. Representation of OE and CE for small (<5 km²) and large (>5 km²) fires for SLSTR and MODIS in the year 2021. (a,b) for MODIS. (c,d) for SLSTR.

In smaller fire events (<5 km²), for both sensors, there was low spatial correspondence in relation to the reference product, with a DC coefficient of 0.277 for MODIS and 0.27 for SLSTR. For the SLSTR, the classifier erroneously detected approximately 1145 km² of unburned area, causing an OE of 66% and a CE of 84%. MODIS also showed a high estimate of CE (85%), with 176.8 km² of correctly classified burned areas, while the SLSTR correctly classified 40.3 km². Overall, SLSTR showed greater sensitivity in the accuracy analysis for small and large fires, with slightly higher error estimates compared to MODIS, especially for small fires. Figure 9 shows the linear regression analysis by a 5 × 5 km proportion for small and large fires in the year 2021.

It was observed that the regressions for the analysis of large fires stood out in relation to small fires. This statement is encouraged by the values of R² and linear coefficient, being slightly better for the estimates of burned areas in large fires with emphasis on MODIS. The SLSTR presented low R² estimates, and high linear coefficient values for both analyses, while the MODIS showed a good performance with a high R² value in the analysis for large fires and moderate R² for small fires in addition to the linear coefficient values practically reaching zero.

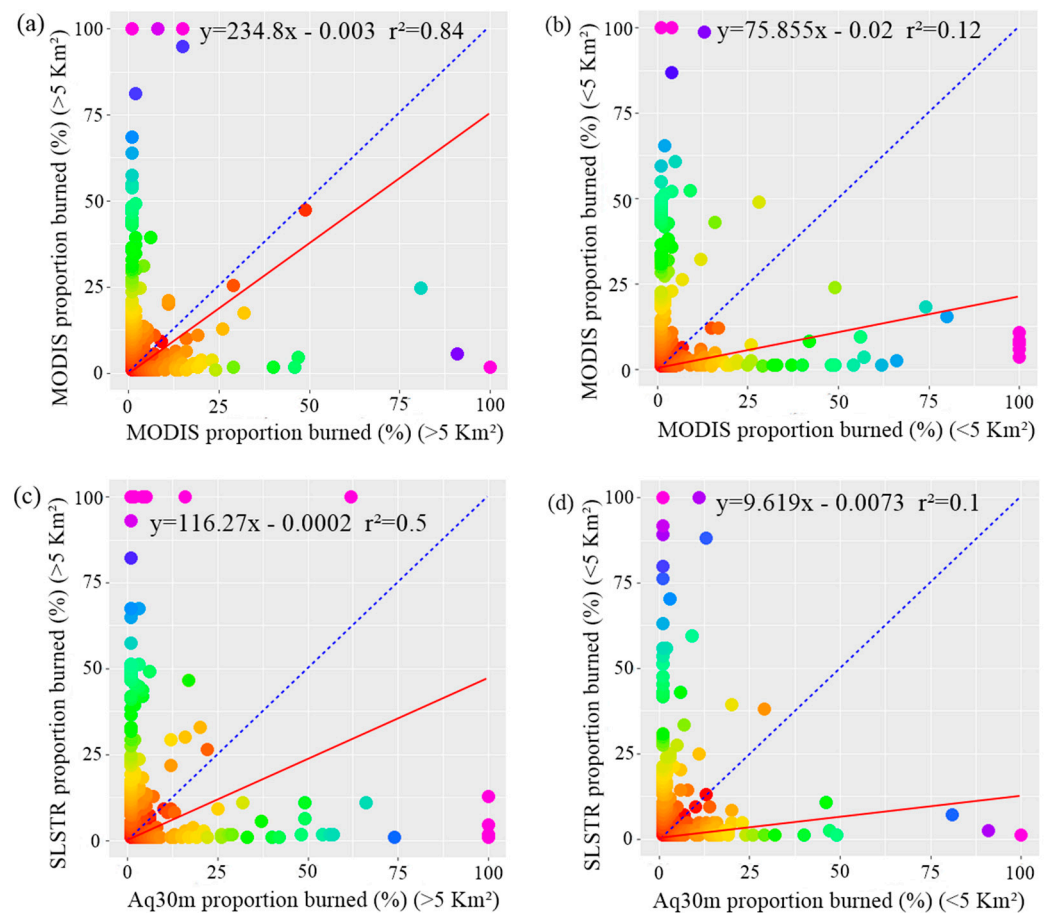


Figure 9. Linear regression by a 5×5 km proportion for small and large fires in the year 2021 for SLSTR and MODIS. (a,c) for small fires. (b,d) for large fires.

4. Discussion

4.1. Sensitivity and Separability of Detection Based on Spectral Characteristics

Differences in spectral separability performance for targets after wildfire events were observed by Lasaponara [62] and Pacheco et al. [31]. The separability estimates shown in Figure 2 are similar to those based on examining data from polar-orbiting satellites [63]. Thus, Lasaponara [62] suggested that these observations may be due to the different types of land cover affected by the fire. Despite this complexity, the most common change is a decrease in reflectance associated with the deposition of black coal which has an almost flat spectrum from VIS to SWIR and contrasts with the reflectance of vegetation and soil [47,64], although white ash deposition and exposure to highly reflective soil can increase post-fire reflectance [65].

Regarding the VIS bands, as discussed in the literature and seen in the separability results shown in this work, the VIS wavelengths have a very poor performance in distinguishing between burned and unburned areas [17,59,66,67]. This is well established, since in this spectral region, the reflectance of dead or senescent vegetation is similar to that of burned vegetation [32,64], in addition to sensitivity to smoke dispersion and other types of aerosols [68], although some studies find them useful for monitoring post-fire regeneration, particularly in areas with bright soils [69].

In the separability analysis, the IR band in both MODIS and SLSTR showed high performance in discrimination of burned areas. The high discriminatory power of the NIR is consistent with the studies by Veraverbeke et al. [70], Smith et al. [64], Pereira [47], and Pacheco et al. [31]. This spectral region has been widely regarded as the best region to detect and map burned areas [67], as this range is strongly reflected by the removal or burning of vegetation, which implies a significant drop in reflectance. Thus, the separability values

presented in Figure 3 were expected for both sensors, since the NIR, both numerically and visually, can detect patterns of abrupt change in vegetation from recent fires. Briefly, the reflectance of burned surfaces is the result of a mixture of exposed soil, unburned vegetation, ash, and coal that are present on the surface after the fire event. In the NIR, vegetation combustion significantly influences the spectral signature of the burned target, generally decreasing the reflectance and consequently increasing the difference in relation to unburned conditions [71,72]. The importance of NIR for discrimination of burned areas is explored in Lizundia-Loiola et al. [73]. The authors implemented an algorithm based on only a single MODIS reflectance band (NIR) to take advantage of the best ground sampling distance of this dataset (250 m/pixel), at the cost of reducing the potential benefits of using other spectral bands, since NIR reflectance has the added benefit of extending the range of sensors for which our algorithm should be suitable for, as the vast majority acquire NIR reflectance (Landsat OLI, MODIS, Sentinel-2 MSI, Sentinel-3 OLCI, Envisat-MERIS, Probe -V).

Despite the SWIR2 and SWIR3 bands presenting moderate performance separability in both sensors (Figure 2), in the literature, the uses of these bands are essential to increase the accuracy and detection in fire mapping by remote sensing. The SWIR1 band in this study presented the best performance in relation to the SWIR2 and SWIR 3 bands, which corresponds to the studies by Schepers et al. [67], Lizundia-Loiola [73], and Pleniou and Koutsias [74], but differs from Veraverbeke et al. [70] and Van Wagtenonk et al. [75]. The SWIR region is strongly absorbed by the water content in vegetation or soil [76]. After a fire, burned areas show high reflectance and transmittance in the SWIR region [77]. Thus, detection using SWIRs (short and long SWIR) tends to decrease, as the distinct spectral signatures of water and burned areas decrease beyond the NIR region. There, water tends to absorb longer wavelengths almost completely, while the reflectance of the burned forest remains fairly constant or shows a slightly increasing trend [78,79]. In implementing the SWIR band for the detection of multi-temporal forest fires in the Rocky Mountains in Mexico, it was observed to have high discriminatory power in changes in post-fire recovery, while Alcaras et al. [80] observed excellent SWIR performance, both in the case of the unitemporal (post-fire) and bitemporal (pre-fire and post-fire in comparison) approaches.

In the studies by Roy et al. [63], the authors observed high separability between burned and unburned observations throughout the day and concluded that the SWIR bands are less affected by the atmosphere than the VIS bands due to their longer wavelengths, in addition to the long provenance for mapping burned area from a variety of sensors in polar orbit (e.g., [41,81,82]). On the other hand, the band separability power of SWIR in the temporal shift detection algorithm has also been widely exploited as an indicator of burn severity, although the sensitivity of these bands has been found to vary geographically [83].

4.2. Analysis of Detection Errors and Relationship with Other Studies in the Mapping of Burned Areas by Satellite

The errors found in the classification of the burned areas were caused by several factors, one of them being the spectral similarity of the burned areas with other surface elements, mainly low albedo bodies. Furthermore, the spatial accuracy of MODIS and SLSTR images was an important agent in reducing data performance when compared to finer resolution images (Landsat). Therefore, this section will discuss the influence of spectral, temporal, and spatial resolution for detecting variability and spatial errors found in MODIS and SLSTR burned area maps.

Some existing results in the literature using images of coarse spatial resolution were in accordance with those obtained in this study. Pulvirenti et al. [84] proposed an automated algorithm based on spectral indices for Sentinel-2 data on forest areas and obtained an average CE of 6.3% and an OE of 12.7%. Likewise, Smiraglia et al. [85] obtained a CE of 33% and an OE of 24% when also exploring the spectral indices. Seydi et al. [86] mapped burned areas with a random forest algorithm, with CE of 8.7% and OE of 9.2%. Libonati et al. [17], using an automatic classification model using MODIS images in the Cerrado,

obtained a CE of approximately 80% and an OE of 30%. Ramo et al. [87] obtained a CE of 99.2% and OE of 95.5% for post-fire sparse vegetation. Santana et al. [88], using MODIS images and its derived products in all Brazilian biomes, found a CE of 42.01% and an OE of 78.03%. Pacheco and Silva Júnior [89] obtained, in the state of Maranhão, OE and CE values of approximately 80%. Franquesa et al. [90] obtained an estimated CE and OE of 19% and 49%, respectively using MODIS MCD64 data, while Katagis and Gitas [91] obtained greater OE (52%) but lower CE (19%) than FireCCI51 (OE = 0.36 and CE = 0.40) in Mediterranean ecosystems. Similarly, Boschetti et al. [56] estimated that MCD64C6 had a CE of 40% and OE of 73%, based on 16-day sampling units in a global analysis.

Van Dijk et al. [92] and Goodwin and Collett [93] reported that the main problems with the incorrect classification of the burned area are related to the spectral variability present in the satellite images due to land use change in relation to agricultural crops, frequently flooded lands, and variations in moisture and soil cover in dark soils. This problem is exacerbated when considering the different numbers of bands between SLSTR and MODIS. This was quite evident in the classification with SLSTR images, since, for this sensor, only four bands (green, red, NIR, and SWIR) were used in the classification. That is, when fewer spectral resources for feature detection are available, the increase of false alarm pixels and overestimations is favored in relation to MODIS, considering the results found that MOD09A1 scenes provide the blue band and four wavelength ranges present in the IR, which probably influenced the lower CE in relation to the SLSTR. Van Dijk et al. [92] found that the NIR and SWIR bands performed exceptionally in reducing false positives, although Filippini [94] got a CE of around 25% and an OE of around 40% in classifying burned areas in Italy and attributed these estimates due to SWIR variability resulting from charcoal removal and vegetation restoration. On the other hand, Hawbaker et al. [29] using MODIS and Landsat showed that the use of red, NIR, SWIR1, SWIR2, and thermal bands were repeatedly effective to map burned areas and fire severity in the USA, with CE and OE rates of 28% and 40%, respectively, when validated with Landsat-derived reference data and 19% and 41%, respectively, when validated with high-resolution commercial satellite imagery.

4.3. Influence of Spatial Resolution and Fire Size

Given the relevance of the fire size, the analysis of this factor is based on general measurements of accuracy and mainly by comparing the accuracy standards for fire sizes above and below 5 km². The comparison between the best detection between SLSTR and MODIS sensors, namely for a higher DC and R², showed that a finer spectral resolution is advantageous for mapping small and large fires. More importantly, the results of this paper show that fire size plays a crucial role in reported accuracy, which is particularly serious for coarse-resolution sensors. Therefore, it is important that the validation of the classification of burned areas includes an assessment of the fire size distribution, as this is very relevant for interpreting accuracy estimates.

The OE, being represented by pixels wrongly classified as unburned areas, presented significant and well-distributed values for the maps generated by both sensors. Fire features with an area smaller than 5 km² mapped by Landsat images were identified as one of the variables for the spatial discrepancy in the comparison between 30 and 500 m. Unburned areas within a fire polygon are common and can significantly alter the differential reflectance when 500 m/pixel GSD imagery is used. In this case, small fragments that are detected as unburned at 30 m/pixel GSD, embedded in the burned area, may be considered as burned at 500 m/pixel GSD, resulting in larger estimation errors. The same behavior happens in isolated pixels of burned areas of the reference product. The very large pixel size may underestimate burned areas detected in finer spatial resolution image pixels, since they may be attenuated by the ground cover inserted in the 25 km² grid. For example, in the case of SLSTR and MODIS, the low spatial resolution of the images generated by the SLSTR and MODIS sensors tended to miss fires that have a fast recovery of vegetation, in addition to spectral mixing problems commonly found at the edges of scars. Therefore, fast

recovery events are the main source of OE in Landsat images. This is true when comparing imaging dates (Table 2) and the spatial distribution of OE and CE (Figure 5), although some singular disparities are important to note. The first one is for the year 2021, which despite the same day of recording the scene for SLSTR and Landsat, there was a higher estimate of OE and CE compared to the MODIS scene.

4.4. Temporal Influence of Recording of SLSTR and MODIS Scenes Compared to Aq30m

The temporal variability between the imagery of the burn between the SLSTR, MODIS, and the reference data can also cause significant OE and CE. The vegetation of the Cerrado biome has a high capacity for post-fire regeneration, which results in the lowest spectral signal of the burned vegetation received by the sensor, especially when imaging occurs many days after the start of the fire. Briefly, the scars of lower intensity detected by orbital sensors can be identified as the vegetation affected by the fire that recovered quickly during the several months after the beginning of the fire. On the other hand, the deposition of charcoal detected by dimming in satellite images is a very specific consequence of the low spectral signal of the burned vegetation; however, it is relatively short-lived. Charcoal is mitigated by wind dispersion or washed off by rain, over a period of a few weeks to a few months after the fire. In 2019, SLSTR recorded the study area 5 days prior to the validation product date, while MODIS recorded 1 day prior. The high estimate of OE found for the SLSTR may be linked to this delay in temporal detection after burning recorded by Landsat, being quantified by the STEC of 0.76. In 2020 and 2021, there was unusual behavior. The temporal proximity of the SLSTR, being represented by a STEC close to zero, was not able to reduce the OE and CE, while the MODIS, with high values of STEC, presented smaller estimates of errors. This behavior may be related to atmospheric conditions such as shadows, cirrus clouds, or aerosols, which interfered in the visibility and detection of the burned area in the SLSTR mosaic, unlike MODIS, where there was probably greater spectral persistence of the vegetation scar signal despite the products being known for atmospheric contamination.

5. Conclusions

The detection of burned areas through the MODIS reflectance product (MOD09A1) showed better performance, which may be related to the greater number of bands used in the classification compared to the SLSTR, being possible to observe through the STEC coefficient that the spectral resolution proved to be the most important parameter compared to the temporal proximity between the burn persistence and the reference product. On the other hand, both sensors showed considerable OE and CE, mainly due to small fires not being detectable in the coarser resolution satellite images.

It was found that the SVM classifier, characterized by its self-adaptability, efficient learning pace, and the adjustment of limited training requirements as the hyperparameters change, was quite reliable in the intelligent processing of data acquired by remote sensing in forest fire studies. It is noteworthy, however, that the interference caused by smoke and other atmospheric conditions adds considerable variability to the spectral characteristics of the burned pixels. This often results in spurious fire events if there is an active fire signal in the spatial vicinity, causing confusion in the algorithm.

The influence of fire spans a wide range of temporal and spatial scales, as well as interpretations of causal factors. Therefore, ecological responses are a challenge for both research and management. However, classifying measurements through remote sensing digital image processing as active or post-fire characteristics is still challenging as fire effects vary temporally and with topography and vegetation, although multiple sources of current remote-controlled sensing data continue to accumulate and increasingly sophisticated techniques are being employed. The methodology used can be useful to map regions of native vegetation affected by fire and the impacts generated by it, in addition to improving methods for monitoring the natural resources of the Cerrado, which may be extended to other biomes. Therefore, research remains on how to infer post-fire land cover charac-

teristics to improve the detection of burned areas under the different specifications and limitations of remote sensing data. For future studies, it is interesting to use and improve techniques for the thermal and fire saturation bands from SLSTR and MODIS data.

Author Contributions: Conceptualization, J.A.d.S.J. and A.d.P.P.; methodology, J.A.d.S.J. and A.d.P.P.; software, J.A.d.S.J. and A.d.P.P.; validation, J.A.d.S.J., A.d.P.P., A.M.R.-A. and R.F.F.H.; formal analysis, J.A.d.S.J., A.d.P.P., A.M.R.-A. and R.F.F.H.; investigation, J.A.d.S.J., A.d.P.P., A.M.R.-A. and R.F.F.H.; resources, J.A.d.S.J. and A.d.P.P.; data curation, J.A.d.S.J.; writing—original draft preparation, J.A.d.S.J.; writing—review and editing, J.A.d.S.J., A.d.P.P., A.M.R.-A. and R.F.F.H.; visualization, J.A.d.S.J., A.d.P.P., A.M.R.-A. and R.F.F.H.; supervision, J.A.d.S.J., A.d.P.P., A.M.R.-A. and R.F.F.H.; project administration, J.A.d.S.J., A.d.P.P., A.M.R.-A. and R.F.F.H.; funding acquisition, J.A.d.S.J., A.d.P.P., A.M.R.-A. and R.F.F.H. All authors have read and agreed to the published version of the manuscript.

Funding: This research was supported by POAIUJA 2021-22 and CEACTEMA from the University of Jaén (Spain), and RNM-282 research group from the Junta de Andalucía (Spain). This work was also supported by Portuguese national funding awarded by FCT—Foundation for Science and Technology, I.P., projects UIDB/04683/2020 and UIDP/04683/2020.

Data Availability Statement: Data supporting the findings of this study are available in the public domain. MODIS data (<https://earthexplorer.usgs.gov/>, accessed on 15 October 2022), Sentinel-3 (<https://scihub.copernicus.eu/>, accessed on 15 October 2022), BDQueimadas (<https://queimadas.dgi.inpe.br/queimadas/aq30m/>, accessed on 15 October 2022).

Conflicts of Interest: The authors declare no conflict of interest.

References

- Frizzo, T.L.M.; Bonizario, C.; Prado Borges, M.; Vasconcelos, H. Uma revisão dos efeitos do fogo sobre a fauna de formações savânicas do Brasil. *Oecologia Aust.* **2011**, *15*, 365–379. Available online: <https://revistas.uffj.br/index.php/oa/article/view/8135> (accessed on 2 November 2021). [[CrossRef](#)]
- Reddington, C.L.; Conibear, L.; Robinson, S.; Knotte, D.; Arnold, S.R.; Spracklen, D.V. Air Pollution from Forest and Vegetation Fires in Southeast Asia Disproportionately Impacts the Poor. *GeoHealth* **2021**, *5*, e2021GH000418. [[CrossRef](#)]
- Anderson, L.O.; Cheek, D.; EOC Aragao, L.; Andere, L.; Duarte, B.; Salazar, N.; Lima, A.; Duarte, V.; Arai, E. Development of a Point-Based Method for Map Validation and Confidence Interval Estimation: A Case Study of Burned Areas in Amazonia. *J. Remote Sens. GIS* **2017**, *6*, 2. [[CrossRef](#)]
- Redin, M.; dos Santos, G.D.F.; Miguel, P.; Denega, G.L.; Lupatini, M.; Doneda, A.; de Souza, E.L. Impactos Da Queima Sobre Atributos Químicos, Físicos E Biológicos Do Solo. *Ciência Florest.* **2011**, *21*, 381–392. [[CrossRef](#)]
- BRASIL, Ministério do Meio Ambiente. O Bioma Cerrado. 2021. Available online: <https://antigo.mma.gov.br/biomas/cerrado.html> (accessed on 2 November 2021).
- Lewinsohn, T.M.; Prado, P.I. How Many Species Are There in Brazil? *Conserv. Biol.* **2005**, *19*, 619–624. [[CrossRef](#)]
- Alencar, A.; Shimbo, J.Z.; Lenti, F.; Balzani Marques, C.; Zimbres, B.; Rosa, M.; Arruda, V.; Castro, I.; Ribeiro, J.P.F.M.; Varela, V.; et al. Mapping Three Decades of Changes in the Brazilian Savanna Native Vegetation Using Landsat Data Processed in the Google Earth Engine Platform. *Remote Sens.* **2020**, *12*, 924. [[CrossRef](#)]
- Strassburg, B.B.N.; Brooks, T.; Feltran-Barbieri, R.; Iribarrem, A.; Crouzeilles, R.; Loyola, R.; Latawiec, A.E.; Oliveira Filho, F.J.B.; Scaramuzza, C.A.D.M.; Scarano, F.R.; et al. Moment of Truth for the Cerrado Hotspot. *Nat. Ecol. Evol.* **2017**, *1*, 0099. [[CrossRef](#)] [[PubMed](#)]
- Simon, M.F.; Grether, R.; de Queiroz, L.P.; Skema, C.; Pennington, R.T.; Hughes, C.E. Recent Assembly of the Cerrado, a Neotropical Plant Diversity Hotspot, by in Situ Evolution of Adaptations to Fire. *Proc. Natl. Acad. Sci. USA* **2009**, *106*, 20359–20364. [[CrossRef](#)]
- Waigl, C.F.; Stuefer, M.; Prakash, A.; Ichoku, C. Detecting High and Low-Intensity Fires in Alaska Using VIIRS I-Band Data: An Improved Operational Approach for High Latitudes. *Remote Sens. Environ.* **2017**, *199*, 389–400. [[CrossRef](#)]
- Chiang, S.-H.; Ulloa, N.I. Mapping and Tracking Forest Burnt Areas in the Indio Maiz Biological Reserve Using Sentinel-3 SLSTR and VIIRS-DNB Imagery. *Sensors* **2019**, *19*, 5423. [[CrossRef](#)]
- Andela, N.; Morton, D.C.; Giglio, L.; Chen, Y.; Van der Werf, G.R.; Kasibhatla, P.S.; DeFries, R.S.; Collatz, G.J.; Hantson, S.; Kloster, S.; et al. A Human-Driven Decline in Global Burned Area. *Science* **2017**, *356*, 1356–1362. [[CrossRef](#)] [[PubMed](#)]
- Chen, Y.; Morton, D.C.; Jin, Y.; Collatz, G.J.; Kasibhatla, P.S.; Van der Werf, G.R.; DeFries, R.S.; Randerson, J.T. Long-Term Trends and Interannual Variability of Forest, Savanna and Agricultural Fires in South America. *Carbon Manag.* **2013**, *4*, 617–638. [[CrossRef](#)]
- Zhang, Y.; Qin, D.; Yuan, W.; Jia, B. Historical Trends of Forest Fires and Carbon Emissions in China from 1988 to 2012. *J. Geophys. Res. Biogeosci.* **2016**, *121*, 2506–2517. [[CrossRef](#)]

15. European Space Agency. Sentinel 3—Data Access and Products. 2015. Available online: https://sentinels.copernicus.eu/documents/247904/1848151/Sentinel3_SLSTR_Data_Access_and_Products.pdf (accessed on 20 October 2022).
16. European Space Agency, ESA. Introducing Sentinel 3. 2022. Available online: https://www.esa.int/Our_Activities/Observing.../Sentinel-3/Introducing_Sentinel-3 (accessed on 20 October 2022).
17. Libonati, R.; DaCamara, C.; Setzer, A.; Morelli, F.; Melchiori, A. An Algorithm for Burned Area Detection in the Brazilian Cerrado Using 4 Mm MODIS Imagery. *Remote Sens.* **2015**, *7*, 15782–15803. [[CrossRef](#)]
18. Sperling, S.; Wooster, M.J.; Malamud, B.D. Influence of Satellite Sensor Pixel Size and Overpass Time on Undercounting of Cerrado/Savannah Landscape-Scale Fire Radiative Power (FRP): An Assessment Using the MODIS Airborne Simulator. *Fire* **2020**, *3*, 11. [[CrossRef](#)]
19. Rodrigues, J.A.; Libonati, R.; Pereira, A.A.; Nogueira, J.M.P.; Santos, F.L.M.; Peres, L.F.; Santa Rosa, A.; Schroeder, W.; Pereira, J.M.C.; Giglio, L.; et al. How Well Do Global Burned Area Products Represent Fire Patterns in the Brazilian Savannas Biome? An Accuracy Assessment of the MCD64 Collections. *Int. J. Appl. Earth Obs. Geoinf.* **2019**, *78*, 318–331. [[CrossRef](#)]
20. Campagnolo, M.L.; Libonati, R.; Rodrigues, J.A.; Pereira, J.M.C. A Comprehensive Characterization of MODIS Daily Burned Area Mapping Accuracy across Fire Sizes in Tropical Savannas. *Remote Sens. Environ.* **2021**, *252*, 112115. [[CrossRef](#)]
21. Potter, C.; Klooster, S.; Huete, A.; Genovese, V.; Bustamante, M.; Guimaraes Ferreira, L.; Zepp, R. Terrestrial Carbon Sinks in the Brazilian Amazon and Cerrado Region Predicted from MODIS Satellite Data and Ecosystem Modeling. *Biogeosciences* **2009**, *6*, 937–945. [[CrossRef](#)]
22. Rodrigues Silva, F.G.; dos Santos, A.R.; Fiedler, N.C.; Paes, J.B.; Alexandre, R.S.; Guerra Filho, P.A.; da Silva, R.G.; Moura, M.M.; da Silva, E.F.; da Silva, S.F.; et al. Geotechnology Applied to Analysis of Vegetation Dynamics and Occurrence of Forest Fires on Indigenous Lands in Cerrado-Amazonia Ecotone. *Sustainability* **2022**, *14*, 6919. [[CrossRef](#)]
23. Santos, F.L.M.; Libonati, R.; Peres, L.F.; Pereira, A.A.; Narcizo, L.C.; Rodrigues, J.A.; Oom, D.; Pereira, J.M.C.; Schroeder, W.; Setzer, A.W. Assessing VIIRS Capabilities to Improve Burned Area Mapping over the Brazilian Cerrado. *Int. J. Remote Sens.* **2020**, *41*, 8300–8327. [[CrossRef](#)]
24. Santana, N.; de Carvalho, O., Jr.; Gomes, R.; Guimarães, R. Burned-Area Detection in Amazonian Environments Using Standardized Time Series per Pixel in MODIS Data. *Remote Sens.* **2018**, *10*, 1904. [[CrossRef](#)]
25. Xu, W.; Wooster, M.J.; He, J.; Zhang, T. First Study of Sentinel-3 SLSTR Active Fire Detection and FRP Retrieval: Night-Time Algorithm Enhancements and Global Intercomparison to MODIS and VIIRS AF Products. *Remote Sens. Environ.* **2020**, *248*, 111947. [[CrossRef](#)]
26. Giglio, L.; Schroeder, W.; Justice, C.O. The Collection 6 MODIS Active Fire Detection Algorithm and Fire Products. *Remote Sens. Environ.* **2016**, *178*, 31–41. [[CrossRef](#)] [[PubMed](#)]
27. Daldegan, G.A.; Roberts, D.A.; de Figueiredo Ribeiro, F. Spectral Mixture Analysis in Google Earth Engine to Model and Delineate Fire Scars over a Large Extent and a Long Time-Series in a Rainforest-Savanna Transition Zone. *Remote Sens. Environ.* **2019**, *232*, 111340. [[CrossRef](#)]
28. Long, T.; Zhang, A.; He, G.; Jiao, W.; Tang, C.; Wu, B.; Zhang, X.; Wang, G.; Yin, R. 30 M Resolution Global Annual Burned Area Mapping Based on Landsat Images and Google Earth Engine. *Remote Sens.* **2019**, *11*, 489. [[CrossRef](#)]
29. Hawbaker, T.J.; Vanderhoof, M.K.; Schmidt, G.L.; Beal, Y.-J.; Picotte, J.J.; Takacs, J.D.; Falgout, J.T.; Dwyer, J.L. The Landsat Burned Area Algorithm and Products for the Conterminous United States. *Remote Sens. Environ.* **2020**, *244*, 111801. [[CrossRef](#)]
30. Padilla, M.; Olofsson, P.; Stehman, S.V.; Tansey, K.; Chuvieco, E. Stratification and Sample Allocation for Reference Burned Area Data. *Remote Sens. Environ.* **2017**, *203*, 240–255. [[CrossRef](#)]
31. Pacheco, A.D.P.; da Silva, J.A., Jr.; Ruiz-Armenteros, A.M.; Faria Henriques, R.F. Assessment of K-Nearest Neighbor and Random Forest Classifiers for Mapping Forest Fire Areas in Central Portugal Using Landsat-8, Sentinel-2, and Terra Imagery. *Remote Sens.* **2021**, *13*, 1345. [[CrossRef](#)]
32. Pereira, A.; Pereira, J.; Libonati, R.; Oom, D.; Setzer, A.; Morelli, F.; Machado-Silva, F.; de Carvalho, L. Burned Area Mapping in the Brazilian Savanna Using a One-Class Support Vector Machine Trained by Active Fires. *Remote Sens.* **2017**, *9*, 1161. [[CrossRef](#)]
33. Oliveira, P.D.S.D. Uso de Aprendizagem de Máquina e Redes Neurais Convolucionais Profundas para a Classificação de Áreas Queimadas em Imagens de Alta Resolução Espacial. Repositorio.unb.br 1 (1). 2019. Available online: <https://repositorio.unb.br/handle/10482/38234> (accessed on 15 October 2022).
34. LeCun, Y.; Bengio, Y.; Hinton, G. Deep Learning. *Nature* **2015**, *521*, 436–444. [[CrossRef](#)]
35. EMBRAPA. Embrapa Cerrados. 2. Ed. Rev. Atual. Brasília, DF: Embrapa Informação Tecnológica. 2021. Available online: <https://www.embrapa.br/cerrados> (accessed on 15 October 2022).
36. INPE. Banco de Dados de Queimadas. 2021. Available online: <http://www.inpe.br/queimadas/bdqueimadas> (accessed on 15 October 2022).
37. European Space Agency, ESA. “User Guides—Sentinel-3 SLSTR—Sentinel Online—Sentinel Online.” Sentinel.esa.int. 2021. Available online: <https://sentinel.esa.int/web/sentinel/user-guides/sentinel-3-slstr> (accessed on 15 October 2022).
38. MOD09A1 v006 MODIS/Terra Surface Reflectance 8-Day L3 Global 500 m SIN Grid Home Page. Available online: <https://lpdaac.usgs.gov/products/mod09a1v006/> (accessed on 10 October 2021).
39. Jensen, J.R. *Introductory Digital Image Processing: A Remote Sensing Perspective*, 2nd ed.; Prentice Hall, Inc.: Upper Saddle River, NJ, USA, 1996.

40. Swain, P.H.; Davis, S.M.; Landgrebe, D.A.; Hoffer, R.M. *Remote Sensing: The Quantitative Approach*; McGraw-Hill International Book Company: New York, NY, USA, 1978; Available online: <https://books.google.com.br/books?id=11U5AAAAIAAJ> (accessed on 15 October 2022).
41. Huang, H.; Roy, D.; Boschetti, L.; Zhang, H.; Yan, L.; Kumar, S.; Gomez-Dans, J.; Li, J. Separability Analysis of Sentinel-2A Multi-Spectral Instrument (MSI) Data for Burned Area Discrimination. *Remote Sens.* **2016**, *8*, 873. [[CrossRef](#)]
42. Li, W.; Fu, H.; Yu, L.; Gong, P.; Feng, D.; Li, C.; Clinton, N. Stacked Autoencoder-Based Deep Learning for Remote-Sensing Image Classification: A Case Study of African Land-Cover Mapping. *Int. J. Remote Sens.* **2016**, *37*, 5632–5646. [[CrossRef](#)]
43. Evans, J.; Murphy, M.; Ram, K. Package “SpatialEco” Type Package Title Spatial Analysis and Modelling Utilities. 2021. Available online: <https://cran.r-project.org/web/packages/spatialEco/spatialEco.pdf> (accessed on 15 October 2022).
44. Vapnik, V. *Statistical Learning Theory*; Wiley: New York, NY, USA, 1998.
45. Pal, M.; Mather, P.M. Support Vector Machines for Classification in Remote Sensing. *Int. J. Remote Sens.* **2005**, *26*, 1007–1011. [[CrossRef](#)]
46. Dragozi, E.; Gitas, I.; Stavrakoudis, D.; Theocharis, J. Burned Area Mapping Using Support Vector Machines and the FuzCoC Feature Selection Method on VHR IKONOS Imagery. *Remote Sens.* **2014**, *6*, 12005–12036. [[CrossRef](#)]
47. Pereira, J.M.C.; Mota, B.; Privette, J.L.; Caylor, K.K.; Silva, J.M.N.; Sá, A.C.L.; Ni-Meister, W. A Simulation Analysis of the Detectability of Understory Burns in Miombo Woodlands. *Remote Sens. Environ.* **2004**, *93*, 296–310. [[CrossRef](#)]
48. Sheykhmousa, M.; Mahdianpari, M.; Ghanbari, H.; Mohammadimanesh, F.; Ghamisi, P.; Homayouni, S. Support Vector Machine versus Random Forest for Remote Sensing Image Classification: A Meta-Analysis and Systematic Review. *IEEE J. Sel. Top. Appl. Earth Obs. Remote Sens.* **2020**, *13*, 6308–6325. [[CrossRef](#)]
49. Hosseini, M.; McNairn, H.; Mitchell, S.; Robertson, L.D.; Davidson, A.; Ahmadian, N.; Bhattacharya, A.; Borg, E.; Conrad, C.; Dabrowska-Zielinska, K.; et al. A Comparison between Support Vector Machine and Water Cloud Model for Estimating Crop Leaf Area Index. *Remote Sens.* **2021**, *13*, 1348. [[CrossRef](#)]
50. Noi, T.P.; Kappas, M. Comparison of Random Forest, K-Nearest Neighbor, and Support Vector Machine Classifiers for Land Cover Classification Using Sentinel-2 Imagery. *Sensors* **2018**, *18*, 18. [[CrossRef](#)]
51. Martins, F.D.; Cunha, A.M.C.; Carvalho, A.S.; Costa, F.G. Grupos de Queimada Controlada Para Prevenção de Incêndios Florestais No Mosaico de Carajás. *Biodivers. Bras.-BioBrasil* **2016**, *3*, 121–134.
52. Li, F.; Bond-Lamberty, B.; Levis, S. Quantifying the Role of Fire in the Earth System—Part 2: Impact on the Net Carbon Balance of Global Terrestrial Ecosystems for the 20th Century. *Biogeosciences* **2014**, *11*, 1345–1360. [[CrossRef](#)]
53. Meyer, D. Package ‘1071’. 2022. Available online: <https://cran.r-project.org/web/packages/e1071/e1071.pdf> (accessed on 20 October 2022).
54. Story, M.; Congalton, R.G. Remote Sensing Brief Accuracy Assessment: A User’s Perspective. *M. Sci. Appl. Res.* **1986**, *52*, 397–399. Available online: https://www.asprs.org/wp-content/uploads/pers/1986journal/mar/1986_mar_397-399.pdf (accessed on 15 October 2022).
55. Fawcett, S.E.; Waller, M.A.; Miller, J.W.; Schwieterman, M.A.; Hazen, B.T.; Overstreet, R.E. A Trail Guide to Publishing Success: Tips on Writing Influential Conceptual, Qualitative, and Survey Research. *J. Bus. Logist.* **2014**, *35*, 1–16. [[CrossRef](#)]
56. Boschetti, L.; Roy, D.P.; Giglio, L.; Huang, H.; Zubkova, M.; Humber, M.L. Global Validation of the Collection 6 MODIS Burned Area Product. *Remote Sens. Environ.* **2019**, *235*, 111490. [[CrossRef](#)] [[PubMed](#)]
57. Strötgen, J. Domain-Sensitive Temporal Tagging for Event-Centric Information Retrieval. Archiv.ub.uni-Heidelberg.de. 2015. Available online: <https://archiv.ub.uni-heidelberg.de/volltextserver/18357/> (accessed on 15 October 2022).
58. Barsi, Á.; Kugler, Z.; László, I.; Szabó, G.; Abdulmutalib, H.M. Accuracy dimensions in Remote Sensing. *Int. Arch. Photogramm. Remote Sens. Spat. Inf. Sci.* **2018**, *XLII-3*, 61–67. [[CrossRef](#)]
59. Tanase, M.A.; Villard, L.; Pitar, D.; Apostol, B.; Petrila, M.; Chivulescu, S.; Leca, S.; Borlaf-Mena, I.; Pascu, I.-S.; Dobre, A.-C.; et al. Synthetic Aperture Radar Sensitivity to Forest Changes: A Simulations-Based Study for the Romanian Forests. *Sci. Total Environ.* **2019**, *689*, 1104–1114. [[CrossRef](#)]
60. Mountrakis, G.; Im, J.; Ogole, C. Support Vector Machines in Remote Sensing: A Review. *ISPRS J. Photogramm. Remote Sens.* **2011**, *66*, 247–259. [[CrossRef](#)]
61. Bahari, N.I.S.; Ahmad, A.; Aboobaidar, B.M. Application of Support Vector Machine for Classification of Multispectral Data. *IOP Conf. Ser. Earth Environ. Sci.* **2014**, *20*, 012038. [[CrossRef](#)]
62. Lasaponara, R. Estimating Spectral Separability of Satellite Derived Parameters for Burned Areas Mapping in the Calabria Region by Using SPOT-Vegetation Data. *Ecol. Model.* **2006**, *196*, 265–270. [[CrossRef](#)]
63. Roy, D.P.; Li, Z.; Giglio, L.; Boschetti, L.; Huang, H. Spectral and Diurnal Temporal Suitability of GOES Advanced Baseline Imager (ABI) Reflectance for Burned Area Mapping. *Int. J. Appl. Earth Obs. Geoinf.* **2021**, *96*, 102271. [[CrossRef](#)]
64. Smith, A.M.S.; Andrew, T. Estimating Combustion of Large Downed Woody Debris from Residual White Ash. *Int. J. Wildland Fire* **2005**, *14*, 245. [[CrossRef](#)]
65. Smith, A.M.S.; Wooster, M.J.; Drake, N.A.; Dipotso, F.M.; Falkowski, M.J.; Hudak, A.T. Testing the Potential of Multi-Spectral Remote Sensing for Retrospectively Estimating Fire Severity in African Savannahs. *Remote Sens. Environ.* **2005**, *97*, 92–115. [[CrossRef](#)]
66. Elhag, M.; Yimaz, N.; Bahrawi, J.; Boteva, S. Evaluation of Optical Remote Sensing Data in Burned Areas Mapping of Thasos Island, Greece. *Earth Syst. Environ.* **2020**, *4*, 813–826. [[CrossRef](#)]

67. Schepers, L.; Haest, B.; Veraverbeke, S.; Spanhove, T.; Vanden Borre, J.; Goossens, R. Burned Area Detection and Burn Severity Assessment of a Heathland Fire in Belgium Using Airborne Imaging Spectroscopy (APEX). *Remote Sens.* **2014**, *6*, 1803–1826. [[CrossRef](#)]
68. Ju, J.; Roy, D.P.; Vermote, E.; Masek, J.; Kovalsky, V. Continental-Scale Validation of MODIS-Based and LEDAPS Landsat ETM+ Atmospheric Correction Methods. *Remote Sens. Environ.* **2012**, *122*, 175–184. [[CrossRef](#)]
69. Siljestrom Ribed, P.; Moreno López, A. Monitoring Burnt Areas by Principal Components Analysis of Multi-Temporal TM Data. *Int. J. Remote Sens.* **1995**, *16*, 1577–1587. [[CrossRef](#)]
70. Veraverbeke, S.; Harris, S.; Hook, S. Evaluating Spectral Indices for Burned Area Discrimination Using MODIS/ASTER (MASTER) Airborne Simulator Data. *Remote Sens. Environ.* **2011**, *115*, 2702–2709. [[CrossRef](#)]
71. da Silva, J.A., Jr.; Pacheco, A.D.P. Análise Do Modelo Linear de Mistura Espectral Na Avaliação de Incêndios Florestais No Parque Nacional Do Araguaia, Tocantins, Brasil: Imagens EO-1/Hyperion E Landsat-7/ETM+. *Anuário Inst. Geociências* **2020**, *43*, 440–450. [[CrossRef](#)]
72. da Silva, J.A., Jr.; Pacheco, A.D.P. Avaliação de Incêndio Em Ambiente de Caatinga a Partir de Imagens Landsat-8, Índice de Vegetação Realçado E Análise Por Componentes Principais. *Ciência Florest.* **2021**, *31*, 417–439. [[CrossRef](#)]
73. Lizundia-Loiola, J.; Gonzalo, O.; Ramo, R.; Chuvieco, E. A Spatio-Temporal Active-Fire Clustering Approach for Global Burned Area Mapping at 250 m from MODIS Data. *Remote Sens. Environ.* **2020**, *236*, 111493. [[CrossRef](#)]
74. Pleniou, M.; Koutsias, N. Sensitivity of Spectral Reflectance Values to Different Burn and Vegetation Ratios: A Multi-Scale Approach Applied in a Fire Affected Area. *ISPRS J. Photogramm. Remote Sens.* **2013**, *79*, 199–210. [[CrossRef](#)]
75. Van Wagendonk, J.W.; Root, R.R.; Key, C.H. 2004. Comparison of AVIRIS and Landsat ETM+ Detection Capabilities for Burn Severity. *Remote Sens. Environ.* **2004**, *92*, 397–408. [[CrossRef](#)]
76. Bastarrika, A.; Chuvieco, E.; Martín, M.P. Mapping Burned Areas from Landsat TM/ETM+ Data with a Two-Phase Algorithm: Balancing Omission and Commission Errors. *Remote Sens. Environ.* **2011**, *115*, 1003–1012. [[CrossRef](#)]
77. Dindaroglu, T.; Babur, E.; Yakupoglu, T.; Rodrigo-Comino, J.; Cerdà, A. Evaluation of Geomorphometric Characteristics and Soil Properties after a Wildfire Using Sentinel-2 MSI Imagery for Future Fire-Safe Forest. *Fire Saf. J.* **2021**, *122*, 103318. [[CrossRef](#)]
78. Oliveira, E.R.; Disperati, L.; Alves, F.L. A New Method (MINDED-BA) for Automatic Detection of Burned Areas Using Remote Sensing. *Remote Sens.* **2021**, *13*, 5164. [[CrossRef](#)]
79. Guz, J.; Sangermano, F.; Kulakowski, D. The Influence of Burn Severity on Post-Fire Spectral Recovery of Three Fires in the Southern Rocky Mountains. *Remote Sens.* **2022**, *14*, 1363. [[CrossRef](#)]
80. Alcaras, E.; Costantino, D.; Guastaferro, F.; Parente, C.; Pepe, P. Normalized Burn Ratio plus (NBR+): A New Index for Sentinel-2 Imagery. *Remote Sens.* **2022**, *14*, 1727. [[CrossRef](#)]
81. García, M.; López, J.; Caselles, V. Mapping Burns and Natural Reforestation Using Thematic Mapper Data. *Geocarto Int.* **1991**, *6*, 31–37. [[CrossRef](#)]
82. Roy, D.P.; Huang, H.; Boschetti, L.; Giglio, L.; Yan, L.; Zhang, H.H.; Li, Z. Landsat-8 and Sentinel-2 Burned Area Mapping—A Combined Sensor Multi-Temporal Change Detection Approach. *Remote Sens. Environ.* **2019**, *231*, 111254. [[CrossRef](#)]
83. Roy, D.P.; Jin, Y.; Lewis, P.E.; Justice, C.O. Prototyping a Global Algorithm for Systematic Fire-Affected Area Mapping Using MODIS Time Series Data. *Remote Sens. Environ.* **2005**, *97*, 137–162. [[CrossRef](#)]
84. Pulvirenti, L.; Squicciarino, G.; Fiori, E.; Fiorucci, P.; Ferraris, L.; Negro, D.; Gollini, A.; Severino, M.; Puca, S. An Automatic Processing Chain for near Real-Time Mapping of Burned Forest Areas Using Sentinel-2 Data. *Remote Sens.* **2020**, *12*, 674. [[CrossRef](#)]
85. Smiraglia, D.; Filipponi, F.; Mandrone, S.; Tornato, A.; Taramelli, A. Agreement Index for Burned Area Mapping: Integration of Multiple Spectral Indices Using Sentinel-2 Satellite Images. *Remote Sens.* **2020**, *12*, 1862. [[CrossRef](#)]
86. Seydi, S.T.; Akhoondzadeh, M.; Amani, M.; Mahdavi, S. Wildfire Damage Assessment over Australia Using Sentinel-2 Imagery and MODIS Land Cover Product within the Google Earth Engine Cloud Platform. *Remote Sens.* **2021**, *13*, 220. [[CrossRef](#)]
87. Ramo, R.; Roteta, E.; Bistinas, I.; Van Wees, D.; Bastarrika, A.; Chuvieco, E.; Van der Werf, G.R. African Burned Area and Fire Carbon Emissions Are Strongly Impacted by Small Fires Undetected by Coarse Resolution Satellite Data. *Proc. Natl. Acad. Sci. USA* **2021**, *118*, e2011160118. [[CrossRef](#)] [[PubMed](#)]
88. Santana, N.C.; de Carvalho, O.A., Jr.; Trancoso Gomes, R.A.; Fontes Guimarães, R. Accuracy and Spatiotemporal Distribution of Fire in the Brazilian Biomes from the MODIS Burned-Area Products. *Int. J. Wildland Fire* **2020**, *29*, 907. [[CrossRef](#)]
89. Pacheco, A.D.P.; Da Silva, J.A., Jr. Análise Espaço-Temporal de Áreas de Queimadas No Estado Do Maranhão a Partir de Imagens MODIS E Classificação Random Forest. *Anuário Inst. Geociências* **2020**, *44*, 36119. [[CrossRef](#)]
90. Franquesa, M.; Lizundia-Loiola, J.; Stehman, S.V.; Chuvieco, E. Using Long Temporal Reference Units to Assess the Spatial Accuracy of Global Satellite-Derived Burned Area Products. *Remote Sens. Environ.* **2022**, *269*, 112823. [[CrossRef](#)]
91. Katagis, T.; Gitas, I.Z. Assessing the Accuracy of MODIS MCD64A1 C6 and FireCCI51 Burned Area Products in Mediterranean Ecosystems. *Remote Sens.* **2022**, *14*, 602. [[CrossRef](#)]
92. Van Dijk, D.; Shoaie, S.; Van Leeuwen, T.; Veraverbeke, S. Spectral Signature Analysis of False Positive Burned Area Detection from Agricultural Harvests Using Sentinel-2 Data. *Int. J. Appl. Earth Obs. Geoinf.* **2021**, *97*, 102296. [[CrossRef](#)]

93. Goodwin, N.R.; Collett, L.J. Development of an Automated Method for Mapping Fire History Captured in Landsat TM and ETM+ Time Series across Queensland, Australia. *Remote Sens. Environ.* **2014**, *148*, 206–221. [[CrossRef](#)]
94. Filipponi, F. Exploitation of Sentinel-2 Time Series to Map Burned Areas at the National Level: A Case Study on the 2017 Italy Wildfires. *Remote Sens.* **2019**, *11*, 622. [[CrossRef](#)]

Disclaimer/Publisher’s Note: The statements, opinions and data contained in all publications are solely those of the individual author(s) and contributor(s) and not of MDPI and/or the editor(s). MDPI and/or the editor(s) disclaim responsibility for any injury to people or property resulting from any ideas, methods, instructions or products referred to in the content.